



# Observations of water vapour and carbon monoxide in the Martian atmosphere with the SWC of PFS/MEX

G. Sindoni\*, V. Formisano, A. Geminale

Istituto di Fisica dello Spazio Interplanetario (IFSI)—INAF, Via del Fosso del Cavaliere, 100, 00133 Roma, Italy

## ARTICLE INFO

### Article history:

Received 3 March 2010  
 Received in revised form  
 6 December 2010  
 Accepted 8 December 2010  
 Available online 28 December 2010

### Keywords:

Mars  
 Atmosphere  
 Carbon monoxide  
 Water vapour  
 Spectroscopy

## ABSTRACT

In the history of Mars exploration its atmosphere and planetary climatology aroused particular interest. In the study of the minor gases abundance in the Martian atmosphere, water vapour became especially important, both because it is the most variable trace gas, and because it is involved in several processes characterizing the planetary atmosphere. The water vapour photolysis regulates the Martian atmosphere photochemistry, and so it is strictly related to carbon monoxide. The CO study is very important for the so-called “atmosphere stability problem”, solved by the theoretical modelling involving photochemical reactions in which the H<sub>2</sub>O and the CO gases are main characters.

The Planetary Fourier Spectrometer (PFS) on board the ESA Mars Express (MEX) mission can probe the Mars atmosphere in the infrared spectral range between 200 and 2000 cm<sup>-1</sup> (5–50 μm) with the Long Wavelength Channel (LWC) and between 1700 and 8000 cm<sup>-1</sup> (1.2–5.8 μm) with the Short Wavelength Channel (SWC). Although there are several H<sub>2</sub>O and CO absorption bands in the spectral range covered by PFS, we used the 3845 cm<sup>-1</sup> (2.6 μm) and the 4235 cm<sup>-1</sup> (2.36 μm) bands for the analysis of water vapour and carbon monoxide, respectively, because these ranges are less affected by instrumental problems than the other ones. The gaseous concentrations are retrieved by using an algorithm developed for this purpose.

The PFS/SW dataset used in this work covers more than two and a half Martian years from Ls=62° of MY 27 (orbit 634) to Ls=203° of MY 29 (orbit 6537). We measured a mean column density of water vapour of about 9.6 pr. μm and a mean mixing ratio of carbon monoxide of about 990 ppm, but with strong seasonal variations at high latitudes. The seasonal water vapour map reproduces very well the known seasonal water cycle. In the northern summer, water vapour and CO show a good anticorrelation most of the time. This behaviour is due to the carbon dioxide and water sublimation from the north polar ice cap, which dilutes non-condensable species including carbon monoxide. An analogous process takes place during the winter polar cap, but in this case the condensation of carbon dioxide and water vapour causes an increase of the concentration of non-condensable species. Finally, the results show the seasonal variation of the carbon monoxide mixing ratio with the surface pressure.

© 2010 Elsevier Ltd. All rights reserved.

## 1. Introduction

In the study of the constituent gases of the Martian atmosphere, water vapour arouses particular interest, both because it is the most variable minor gas and because it is involved in many processes characterizing the planetary atmosphere. In fact, the water vapour photolysis controls the Mars atmosphere photochemistry, producing odd hydrogen species, such as H, OH, HO<sub>2</sub> and H<sub>2</sub>O<sub>2</sub>. The latest mean global models of Mars photochemistry were calculated by Nair et al. (1994) and Krasnopolsky (1995).

The carbon monoxide (CO), produced by the CO<sub>2</sub> photodissociation, is strictly related to water vapour not only by photochemical causes, such as the CO<sub>2</sub> catalysed recombination (CO + OH → CO<sub>2</sub> + H),

but also by dynamical effects. The water vapour is a condensable species, while the carbon monoxide is a non-condensable one, so they respond differently to atmospheric processes.

The first observations of Mars atmosphere composition were made using ground-based instruments in the first 1960s (Spinrad et al., 1963). About the seasonal evolution of water vapour, the first dataset was provided by the Echelle-Coudé scanner at McDonald Observatory during the period between 1972 and 1974 (Barker, 1976) and later by the MAWD spectrometer on board the Viking 1 lander using the 1.38 μm absorption band. The main result obtained from this experiment was the coverage of the complete seasonal cycle on Mars, showing a variability of water vapour abundance from a few up to about 100 pr. μm (precipitable microns). These results suggested a water vapour exchange between the atmosphere and the superficial reserves, as permanent and seasonal polar caps and regolith, and a clear transport from north to south caused by the global circulation (Jakosky and Farmer, 1982).

\* Corresponding author. Tel.: +39 0645488511.

E-mail address: [giuseppe.sindoni@ifsi-roma.inaf.it](mailto:giuseppe.sindoni@ifsi-roma.inaf.it) (G. Sindoni).

At the end of the 1980s and in the 1990s data acquired by new spacecrafts were available. The ISM spectrometer on board the *Phobos 2* measured a mean column density of  $9 \pm 3$  pr.  $\mu\text{m}$  in the south and of  $12 \pm 3$  pr.  $\mu\text{m}$  in the north (Rosenqvist et al., 1992). In 1997 the photocamera on board the lander *Pathfinder* measured photometrically a column density of  $6 \pm 4$  pr.  $\mu\text{m}$  in the Ares Vallis region at  $L_s = 150^\circ$  and a water vapour confinement in the boundary layer (1–3 km upon the surface) (Titov et al., 1999).

In the period between 1999 and August 2004 the “Thermal Emission Spectrometer” (TES) on board the Mars Global Surveyor acquired spectra covering the spectral band 20–45  $\mu\text{m}$ . These data cover more than three Martian years always at 14:00 local time (Smith, 2004). A reanalysis of TES acquired spectra has lowered the water vapour results by 30% (Smith, 2008). The whole seasonal coverage includes three summers of the northern hemisphere and shows a maximum water vapour column density from 55 to 80 pr.  $\mu\text{m}$  varying in the three different years. Recently, Smith et al. (2009) published also the water vapour results obtained from MRO/CRISM data.

Since January 2004 Europe has been contributing to the Mars exploration with *Mars Express*. Water vapour in the atmosphere has been studied by the three spectrometers on board: OMEGA (Encrenaz et al., 2005; Melchiorri et al., 2007), SPICAM (Fedorova et al., 2006) and PFS (Fouchet et al., 2007; Tschimmel et al., 2008).

Although water vapour and a few atmospheric species involved in Mars photochemistry, such as  $\text{O}_3$  (Fast et al., 2009),  $\text{H}_2\text{O}_2$  (Encrenaz et al., 2008) and the  $\text{O}_2$  (Altieri et al., 2009; Krasnopolsky, 2006), were observed and studied with a close examination, we do not know much about the carbon monoxide. Regarding the CO study in the Mars atmosphere, Krasnopolsky (2006) published a paper in which the CO mixing ratio variations are shown as observed from Earth with the IRTF/CSHELL instrument using the 1.57  $\mu\text{m}$  band spectroscopy. Another paper was published by Encrenaz et al. (2006) about the study of the CO concentration variations over Hellas region as observed by OMEGA instrument on board the Mars Express, but the first description of the seasonal dependence of the carbon monoxide mixing ratio over a wide latitude range was given by Smith et al. (2009) from CRISM data. Recently also a first paper on the CO observations from PFS-MEX data was published by Billebaud et al. (2009), but the dataset was rather limited.

The study of carbon monoxide is of primary importance for the so-called “stability problem” of the Mars atmosphere. In fact the  $\text{CO}_2$  dissociation in CO and O by photolysis should destroy the whole atmosphere in 6000 years. Then, the CO is recombined forming again  $\text{CO}_2$  thanks to the catalysis of  $\text{H}_2\text{O}$  photolysis products.

The lack of many simultaneous measurements of water vapour and carbon monoxide makes their comparison an issue of great interest for the understanding of photochemical and dynamical processes involved in the Mars planetary atmosphere. So the aim of this work is to investigate these two atmospheric species and their connections.

In this paper we present the results of water vapour and carbon monoxide concentration in the Mars atmosphere using spectra acquired by the PFS SW channel for more than two Martian years. In Section 2 we present a brief instrument and dataset description. In Section 3 we discuss the retrieval algorithm, and finally in Section 4 we show the experimental results, discussing them in Section 5.

## 2. Dataset

### 2.1. The PFS instrument

The Planetary Fourier Spectrometer (PFS) is an instrument optimized for atmospheric studies and it is described in detail by Formisano et al. (2004, 2005). It covers the IR spectral range from 1.2 to 45  $\mu\text{m}$  and it consists of two different channels: the Short

Wavelength Channel (SW), which measures the reflected light from the planet, and the Long Wavelength Channel (LW), which is sensitive to the emitted light from the planet surface. The spatial resolution is about 8 and 13 km for the SW and LW channel, respectively, from an altitude of 300 km. The SW channel uses a PbSe detector passively cooled to 200–220 K, whereas the LW channel detector is a pyroelectric device ( $\text{LiTaO}_3$ ), which works at room temperature. The interferogram is sampled using a reference laser diode signal.

Apodized spectra were used for this work because of their noise reduction and the decrease of the overshooting effect in the red wing that is typical for the PFS instrumental function. The spectral response function of the instrument has a FWHM of  $2.04 \text{ cm}^{-1}$  with Hamming apodization and a sampling step of  $1.05 \text{ cm}^{-1}$ . The loss of spectral resolution caused by the use of apodized spectra is not a problem, because the abundance analysis is done on absorption bands and not on single lines.

Regarding the in-flight performance, there are three causes for instrumental uncertainties that have to be taken into account: problems with radiometric calibrations, random noise due to the detector and AD converter and the influence of spacecraft vibrations (Giuranna et al., 2005). These instrumental uncertainties may alter the effective depth of the absorption lines, leading to errors in the estimations of gas abundance. In order to reduce the noise and thus to improve the signal-to-noise ratio (S/N), we used average spectra and, to be independent on the absolute calibration, we analysed the relative band depths. As inferred by Comolli and Saggin (2005) and confirmed by Giuranna et al. (2007) the spacecraft vibrations affect only the level of the continuum leaving unaltered the relative depth of the atmospheric absorption lines.

### 2.2. Observations

The PFS/SW dataset used in this work covers more than two and a half Martian years from  $L_s = 62^\circ$  of MY 27 (orbit 634) to  $L_s = 203^\circ$  of MY 29 (orbit 6537). For the creation of a single mean spectrum several measurements have to be averaged. This purpose is achieved by averaging spectra in two different ways, making two kinds of datasets. The first, called in this paper “orbital dataset”, is obtained by choosing the ideal number of measurements to average in order to represent the best compromise between the signal-to-noise ratio increase and the maintenance of a good spatial resolution: for the  $\text{H}_2\text{O}$  analysis 15 individual measurements have been averaged, whereas for the CO, the relative band being much weaker (see Section 3), it was necessary to average 50 single measurements. For a single orbit, the mean spectra were built by shifting by 10 measurements from an average to the next one: for example, 1–15, 11–25, 21–35, ..., (for the  $\text{H}_2\text{O}$ ), or 1–50, 11–60, 21–70, ..., (for the CO) and so on. In this way 42,935 mean spectra have been generated for the water vapour analysis and 36,174 mean spectra for the carbon monoxide analysis. The second kind of dataset, called in this paper “bin dataset”, is obtained by averaging spectra in square bins of  $5^\circ$  Solar Longitude ( $L_s$ )  $\times$   $5^\circ$  Latitude for seasonal behaviour studies and in square bins of  $10^\circ$  Longitude  $\times$   $10^\circ$  Latitude for geographic distribution studies. The Latitude vs Longitude bin averages are calculated separately for each of the four seasons: northern Spring ( $L_s = 0\text{--}90^\circ$ ), Summer ( $L_s = 90\text{--}180^\circ$ ), Fall ( $L_s = 180\text{--}270^\circ$ ) and Winter ( $L_s = 305\text{--}360^\circ$ ). Since the aim of our work is the study of the average behaviour of  $\text{H}_2\text{O}$  and CO, data from  $L_s = 270^\circ$  to  $305^\circ$  were excluded, because they are affected by the global-encircling dust storm occurred during the MY 28. In this way we have 2592 mean spectra for the Latitude vs  $L_s$  studies and 648 mean spectra for each season of the Latitude vs Longitude studies.

Obviously, the number of averaged spectra in a single bin is not constant and varies from a minimum of 1 to a maximum of 1277 with a mean value of about 213 for the seasonal study bin dataset

(Fig. 1) and of 208 (Spring), 256 (Summer), 74 (Fall) and 159 (Winter) for the geographical study dataset (Fig. 2).

It is necessary to make two different kinds of dataset to optimize the S/N ratio according to the study aim. The best S/N ratio is obtained in the bin dataset, but this averaging method causes the loss of important information linked to the mean spectrum, such as temporal or orbital information. Therefore, the bin dataset is used when we have to investigate only the seasonal and geographical mean trends of the gaseous concentrations, while the orbital

dataset, keeping the orbital information, allow us to investigate variations on relatively small scales, although with a poorer S/N ratio.

### 3. Analysis procedure

Although there are several H<sub>2</sub>O and CO absorption bands in the spectral range covered by PFS, we used the 2.6  $\mu\text{m}$  ( $3845\text{ cm}^{-1}$ ) band for the water vapour and the 2.36  $\mu\text{m}$  ( $4235\text{ cm}^{-1}$ ) band for the CO analysis, because these ranges are less affected by instrumental problems respect to other ones, and are out of the thermal range limit, avoiding in this way calibration problems due to thermal inversions in the PFS/SWC spectrum (see Section 3.4).

In order to retrieve the H<sub>2</sub>O and CO concentration in the Mars atmosphere, we developed an analysis algorithm. The procedure carried out can be described in several points:

1. Reading of the averaged spectrum and its geometry data.
2. Wavelength grid correction.
3. Extraction of a vertical temperature and pressure profile from the Mars Climate Database (MCD, version 4.2).
4. Creation of synthetic spectrum by a line-by-line calculation of monochromatic opacities for CO<sub>2</sub>, H<sub>2</sub>O (considering the saturation level of water, as defined in Section 3.2) and CO. The obtained transmittance spectrum is multiplied with the solar spectrum and convolved with the PFS instrumental function.
5. Division of the averaged PFS spectrum and of the synthetic spectrum by their own specific defined continuum (normalization).

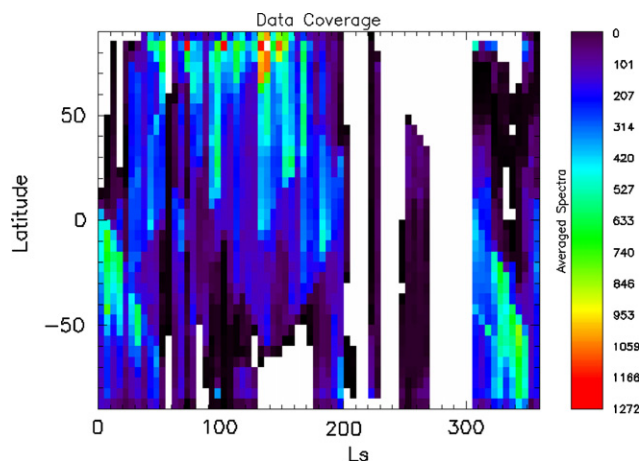


**Fig. 1.** Data coverage for the 5° Ls vs 5° Latitude dataset. Data affected by the global-encircling dust storm of MY 28 (Ls=270–305°) were excluded. The mean number of averaged spectra in a single bin is 213. White bins indicate no data.

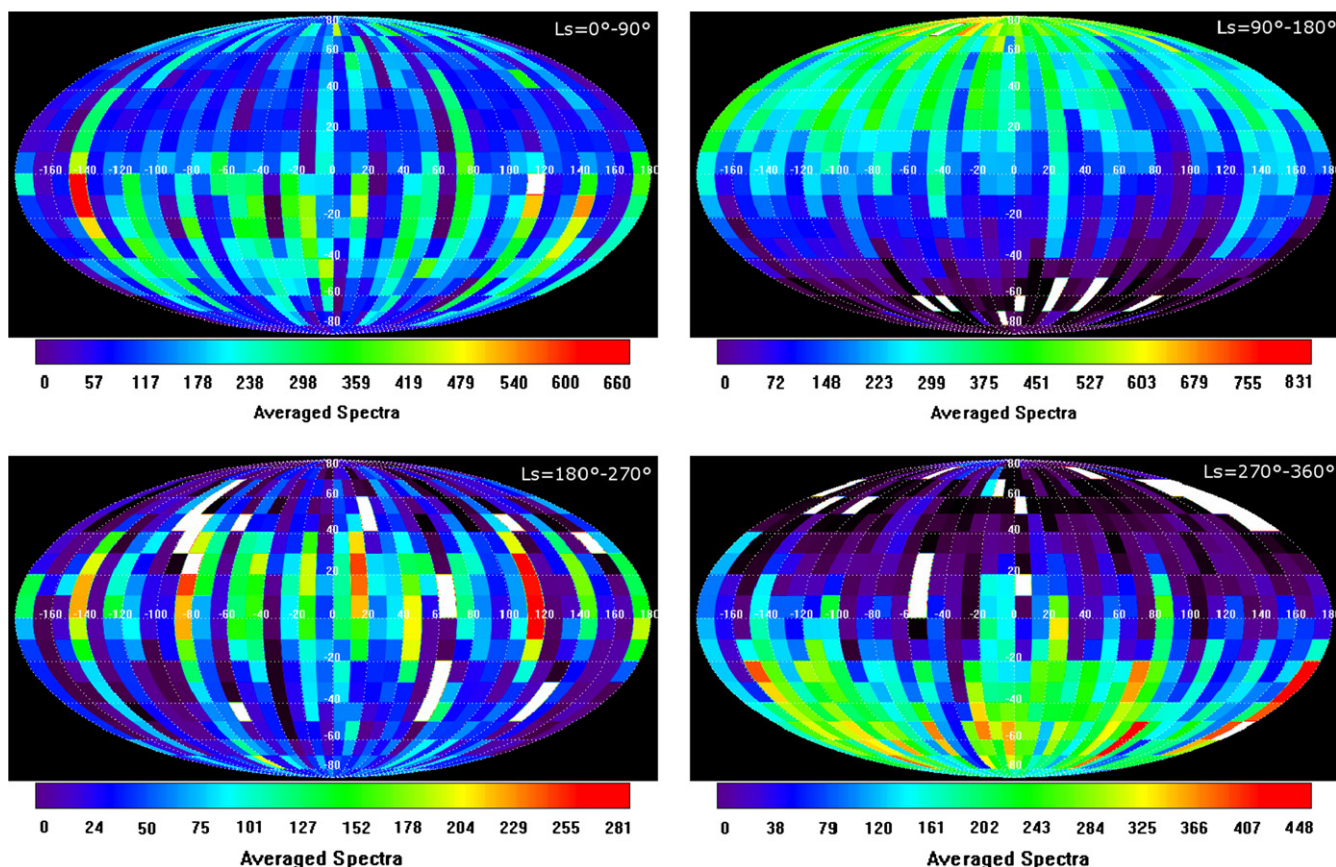


**Fig. 2.** Data coverage for the 10° Longitude vs 10° Latitude dataset for the four seasons: northern Spring (Ls=0–90°), Summer (Ls=90–180°), Fall (Ls=180–270°) and Winter (Ls=305–360°). Data affected by the global-encircling dust storm of MY 28 (Ls=270–305°) were excluded. The mean number of averaged spectra in a single bin is 208 for Ls=0–90°, 256 for Ls=90–180°, 74 for Ls=180–270° and 159 for Ls=270–360°. White bins indicate no data.

## 6. Finding the H<sub>2</sub>O and CO mixing ratio in a fitting loop using a $\chi^2$ minimization.

In the synthetic spectra we considered a fixed value of 0.10 for the dust and ice optical depth, respectively, at 1100 and 825 cm<sup>-1</sup>, with an exponential vertical distribution of particles. This value of optical depths represents the typical Martian conditions out of the dust storm periods (Smith, 2004; Esposito et al., 2006). The properties of dust as a function of wavenumber are those proposed by Ockert-Bell et al. (1997), whereas for water ice we used infrared refractive indices published by Hansen (1999). The grain size distribution used for the aerosols is that described in the model by Clancy et al. (2003). The error related to having neglected variations in the aerosols opacity is evaluated in Section 3.6.

### 3.1. Wavelength grid correction

The wavelength sampling in the averaged measured spectra can be lightly shifted because of the small temporal variations in the laser diode temperature and in the pendulum motion. Then, it is necessary to follow a correction procedure for the spectrum grid. The correction is done for each individual spectrum using a reference synthetic spectrum, which contains 300 ppm of H<sub>2</sub>O and 800 ppm of CO: in this way the exact wavelength of each absorption line is well defined.

The procedure consists in the choice of three minima, representing the position in wavelength of three absorption lines in the observed and synthetic spectra in the spectral range in which the absorption band of interest is contained. The correction factor for the wavelength grid is the mean value of the ratio between the  $w_n$  (wavenumber) positions in the measured spectrum ( $w_{nm}$ ) and the corresponding ones in the synthetic spectrum ( $w_{ns}$ ), i.e.

$$corr = \frac{\sum_{i=1}^3 w_{nm_i} / w_{ns_i}}{3}$$

Averaging the three values is necessary because the correction factor can sometimes be slightly different over the whole spectral range considered. Therefore, in order to obtain the corrected spectrum it is sufficient to divide the old wavelength grid by the correction factor.

The correction factor ranges from 1.00000 to 1.00046, with a mean value of  $1.00018 \pm 0.00008$  and a peak value of the histogram distribution of  $1.00015 \pm 0.00015$ .

### 3.2. The synthetic spectrum

To compute synthetic spectra, geometry data (Latitude, Longitude, Ls, Local Time and Altimetry) of the individual mean spectrum have been used as input for the MCD. From these coordinates, the Global Circulation Model (GCM) provides a vertical temperature and pressure profile with 65 layers. The vertical resolution of the model decreases with altitude, going from about 400 m close to the surface to 7 km at 115 km. Consequently the temperature profile determines the saturation water vapour pressure  $p_s$  over ice (given in Pa), according to the formula by Marti and Mauersberger (1993)

$$\log p_s = -\frac{2663.5 \pm 0.8}{T} + (12.537 \pm 0.011)$$

The atmospheric modelling was performed using the approach of Ignatiev et al. (2005). Synthetic spectra are calculated line-by-line using the absorption coefficients extracted from precalculated gaseous opacities for the temperature and pressure profile of interest. The spectral lines are extracted from the molecular spectroscopic database HITRAN 2004 (Rothman et al., 2005). We have to keep in mind that since this database was created for the Earth's atmosphere, the correction for an atmosphere dominated by CO<sub>2</sub> (Mars case) is

done using a broadening parameter varying between 0.9 and 1.9 from line to line (Gamache et al., 1995). In our case the broadening factor is set to 1.3, as done by Fedorova et al. (2006).

The transmittance spectrum is calculated considering a specific gas (H<sub>2</sub>O or CO) mixing ratio, which is the tuning parameter in the retrieval algorithm. Variations of the CO<sub>2</sub> abundance in the atmosphere are considered as surface pressure variations (taken from the MCD model) rather than mixing ratio variations, which is assumed to be 0.9532. Finally, the transmittance spectrum obtained in this way is multiplied by a high-resolution solar spectrum (Fiorenza and Formisano, 2005) and convolved with the apodized instrumental function.

### 3.3. Spectra normalization

In order to use the relative band depths, it is necessary to normalize the spectrum to its continuum in the spectral region where the absorption bands of interest are present. This purpose is achieved using the approach suggested by Tschimmel et al. (2008). In this way we obtain a normalized synthetic spectrum  $N_{syn}(\lambda)$  and a normalized measured spectrum  $N_{PFS}(\lambda)$  in the spectral ranges from 3780 to 3950 cm<sup>-1</sup> and 4160 to 4300 cm<sup>-1</sup> for analysis of water vapour and carbon monoxide concentration, respectively.

The spectral continuum, both for the measured and the synthetic spectrum, is defined as a piecewise function  $C(\lambda)$ , linear between two local maxima. The  $C(\lambda)$  function is chosen in order to take account of the possible variations of the instrumental behaviour and the different spectral characteristics of the albedo in the two spectral ranges considered for the H<sub>2</sub>O and CO analysis (Fig. 3). A local maximum is defined as the spectral point  $\lambda_M$  which has a higher radiance than its five adjacent spectral points, for the H<sub>2</sub>O analysis, and higher than its three adjacent spectral points, for the CO analysis. The choice of the best number of such spectral points for the continuum definition represents the most reliable result obtained from several tests performed using a different number of spectral point steps. For each step, the best fit ( $\chi^2$ ) between the observed and the synthetic spectrum gives us the best estimate of the number of spectral points to be considered in order to have the best continuum definition.

Mathematically, the normalized spectrum is generated by

$$N(\lambda) = \frac{I(\lambda)}{C(\lambda)}$$

where  $N(\lambda)$  is the normalized spectrum,  $I(\lambda)$  is the radiance spectrum and  $C(\lambda)$  is the continuum. Examples of normalized spectra are shown in Fig. 4 (black line), together with the best fit synthetic spectrum (red line).

### 3.4. Best fit procedure

In the best fit procedure for measured and synthetic spectra the mixing ratio of the atmospheric component (H<sub>2</sub>O or CO) is the resulting variable parameter. In the case of water vapour band, the mixing ratio is considered constant at altitudes below the condensation level and equal to the saturation mixing ratio above it, whereas for the CO analysis a constant distributed vertical profile is considered. Therefore, the synthetic spectrum has to be calculated in each step of the fitting loop in order to keep into account the changing of the saturation level due to the variable H<sub>2</sub>O content. The fit criterion is the minimization of the  $\chi^2$  parameter, weighed by the instrumental noise and defined as

$$\chi^2 = \frac{\sum_{i=1}^{np} (N_{PFS}(\lambda_i) - N_{syn}(\lambda_i))^2}{np(NER/lcont/(\sqrt{nm}))^2}$$

where the sum is extended on all the points of the normalized spectra in the considered spectral range,  $np$  is the number of these

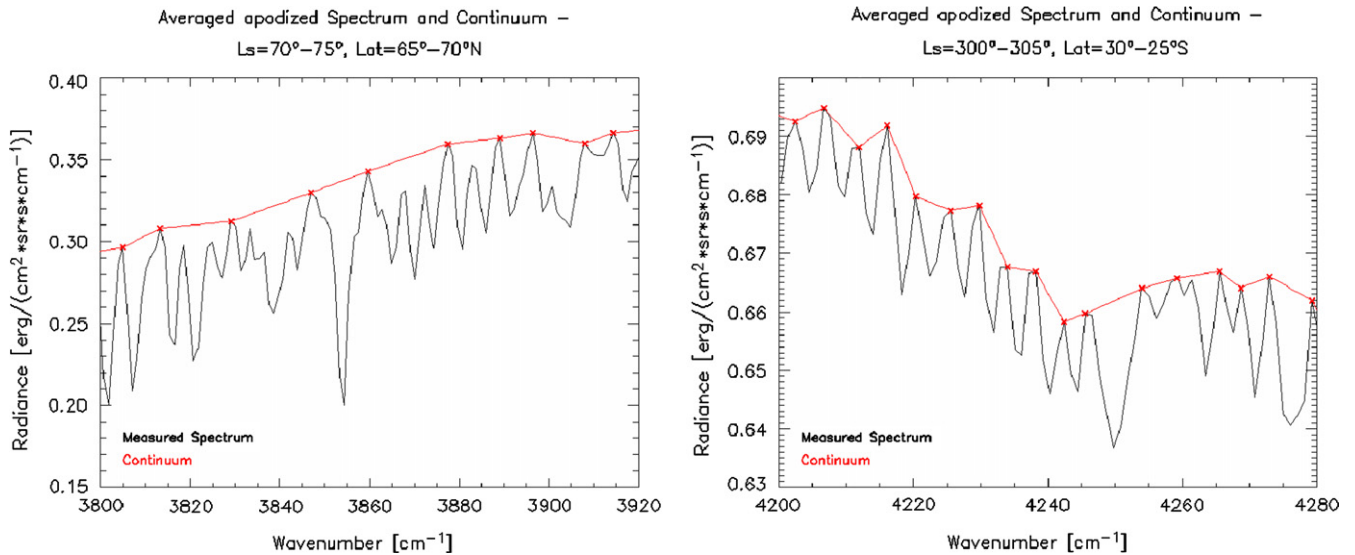


**Fig. 3.** Examples of continuum definition for PFS measured spectra in the absorption band spectral ranges for the H<sub>2</sub>O (left) and the CO (right). The black line is the measured spectrum and the red line is its continuum. The crosses are the spectral point used for the continuum definition. (For interpretation of the references to colour in this figure legend, the reader is referred to the web version of this article.)

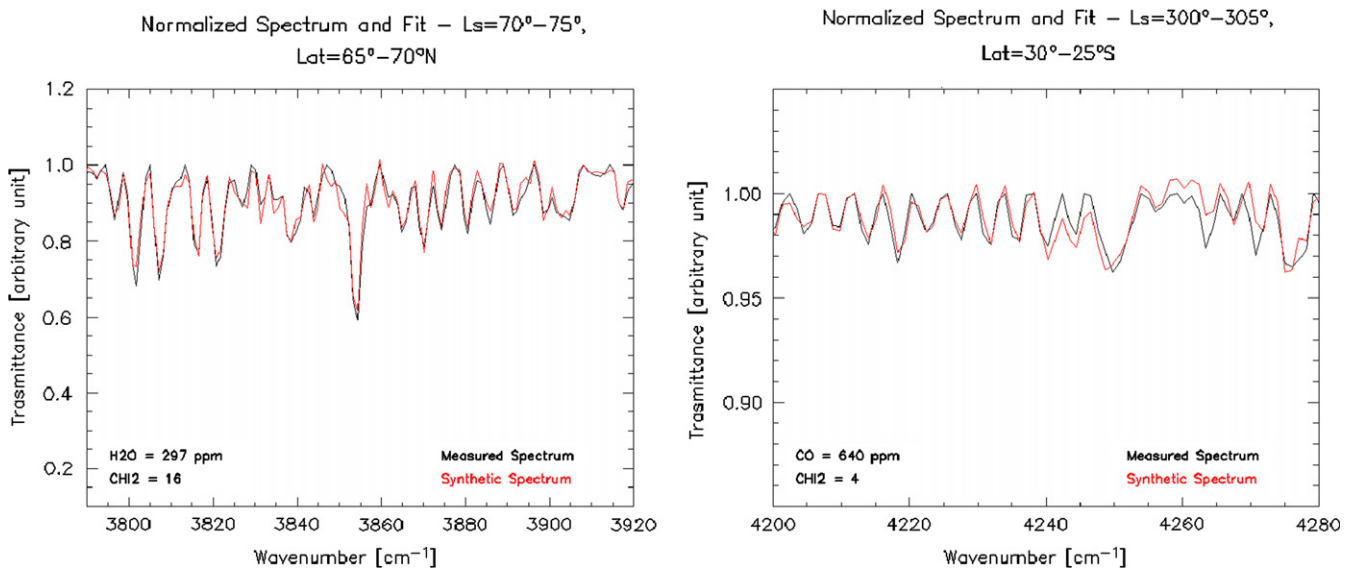


**Fig. 4.** Left-panel: Spectral fit example of the water vapour absorption band for an averaged spectrum (normalized to its continuum), corresponding to 200 single spectra selected into the bin Ls=70–75°, Lat=65–70°N. The retrieved mixing ratio is 297 ppm with a minimum  $\chi^2$  of 16 (over 130 sampling points). Right-panel: Spectral fit example of the carbon monoxide absorption band for an averaged spectrum (normalized to its continuum), corresponding to 243 single spectra selected into the bin Ls=300–305°, Lat=25–30°S. The retrieved mixing ratio is 640 ppm with a minimum  $\chi^2$  of 4 (over 40 sampling points).

points, the *NER* (Noise Equivalent Radiance) (Giuranna et al., 2005) is assumed to have its mean value in the considered range (0.023 and 0.035  $\text{erg s}^{-1} \text{cm}^{-1} \text{sr}^{-1} \text{cm}$ , for the H<sub>2</sub>O and the CO, respectively), *lcont* is the mean continuum radiance in the spectral range and *nm* is the number of the measured averaged spectra. We applied this procedure to a spectral range where the absorption band is stronger and the influence of the solar spectrum is not too strong, i.e. the 3785–3925  $\text{cm}^{-1}$  range for the H<sub>2</sub>O band and the 4200–4245  $\text{cm}^{-1}$  for the CO band.

The synthetic spectrum calculation and its normalization are iterated in a cycle that use a  $\chi^2$  minimization method. The minimum  $\chi^2$  provides the fit quality.

Fig. 4 (left-panel) shows an example of good quality spectral fit of the H<sub>2</sub>O absorption band for an averaged spectrum,

corresponding to 200 single spectra selected within the bin Ls=70–75°, Lat=65–70°N. The vertical atmospheric profiles have been calculated for a latitude of 68.2°N and a longitude of 21.4°E, during Ls=72.9° and a solar local time (Lt) of 8.82. In this case the analysis algorithm gives us a mixing ratio of 297 ppm.

Fig. 4 (right-panel) shows an example of good quality spectral fit of the CO absorption band for an averaged spectrum, corresponding to 243 single spectra selected within the bin Ls=300–305°, Lat=25–30°S. The vertical atmospheric profiles have been calculated for a latitude of 27.5°S and a longitude of 10.6°W, during Ls=301.9° and a solar local time (Lt) of 10.63. In this case the analysis algorithm gives us a mixing ratio of 640 ppm.

However, in spite of the good quality fit, some features, as for example those around 3830 and 3850  $\text{cm}^{-1}$  in Fig. 4 (left-panel),

and those around 4245 and 4260  $\text{cm}^{-1}$  in Fig. 4 (right-panel), remain not well fitted. These features are common to almost all the spectra and their origin has probably to be found in a wrong line broadening factor in the model, in systematic instrumental features or in an unknown contribution of other atmospheric components.

When the averaged measured spectrum radiance level is too low, resulting in a very low signal-to-noise ratio, or when particular albedo features do not allow a correct continuum definition, it is not possible to obtain a good fit. Therefore, results obtained with a poor fit quality will be excluded a posteriori using a selection method that takes into account the  $\chi^2$  value. The  $\chi^2$  histogram distribution reveals a peak in correspondence of a value of 1.5 for the  $\text{H}_2\text{O}$  retrieval and of 2.5 for the CO retrieval, but with a less broad distribution for the last one. The  $\chi^2$  threshold (50 and 25 for the  $\text{H}_2\text{O}$  and the CO band fit, respectively) was chosen in order to strike a balance between the maintenance of a relevant data coverage and a sufficiently good fit quality (Fig. 5). In this way we discarded about 25% of the water vapour data and about 20% of the carbon monoxide data, mostly relating to the night (winter) polar regions, which have a very low signal-to-noise ratio.

The presence of another CO absorption band in the PFS/SWC spectrum, around 2150  $\text{cm}^{-1}$ , allows sometimes the comparison between concentration values obtained from the two different band fits. However, this band in the thermal region of the spectrum, although it is more intense than the other one, hides some analysis problems. The main problem is the calibration of the thermal region of the spectrum, because it is a very complex task when in the spectra there are one or more “thermal inversions”, which depend on the relative temperature between Mars and the detector. In fact, in the thermal radiation range (up to 2900  $\text{cm}^{-1}$ ), the PFS/SW channel is sensitive to the difference of temperature between the emitting source (Mars) and the detector temperature (Giuranna et al., 2005). So, when Mars becomes hotter or cooler than the detector, one or more “phase jumps” occur and they prevent a good spectrum calibration. Unfortunately, we have not still a stable algorithm able to perform this kind of phase correction, therefore spectra affected by thermal inversions can not be used in the retrieval analysis.

In some cases, in which it was possible to apply the same analysis procedure described above (without spectrum normalization), we have compared results from the two bands (an example is shown in Fig. 6). The retrievals obtained from the two bands, analysing the same spectra, differ by about 6%. The result of this comparison validates the method used for the 4200–4245  $\text{cm}^{-1}$  band.

### 3.5. Corrections of CO values a posteriori

The PFS/SWC spectrum has a spectral modulation, due to instrumental problems, centred at about 2  $\mu\text{m}$  (5000  $\text{cm}^{-1}$ ) which starts from about 4000  $\text{cm}^{-1}$ , and therefore it affects the CO absorption band (4235  $\text{cm}^{-1}$ ). Comolli and Saggin (2005) suggested that the modulation affects only the spectral continuum level without changing the relative depth of the spectral features. Therefore the normalization procedure should correct this effect and the mixing ratio values should be independent on the spectral continuum slope. In order to test a possible effect of the 2  $\mu\text{m}$  spectral modulation on the CO band depth we considered the good quality spectral fit ( $\chi^2 < 25$ ) of the “orbital dataset” and we studied the mixing ratio values as a function of the slope of the spectral continuum in the CO band spectral range. Fig. 7 shows the retrieved values for the CO mixing ratio (each point is the average of CO

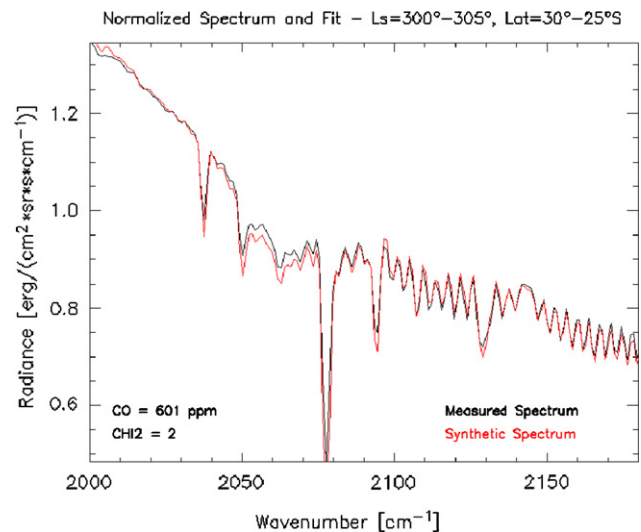


Fig. 6. Spectral fit example of the carbon monoxide absorption band in the range 2000–2180  $\text{cm}^{-1}$  for an averaged spectrum, corresponding to 243 single spectra selected into the bin  $L_s=300\text{--}305^\circ$ ,  $Lat=25\text{--}30^\circ\text{S}$ . The retrieved mixing ratio is 601 ppm with a minimum  $\chi^2$  of 2. We compare this result with the one obtained in Fig. 4, referring to the same spectrum. We note that the difference in the retrieved concentration is about 6%.

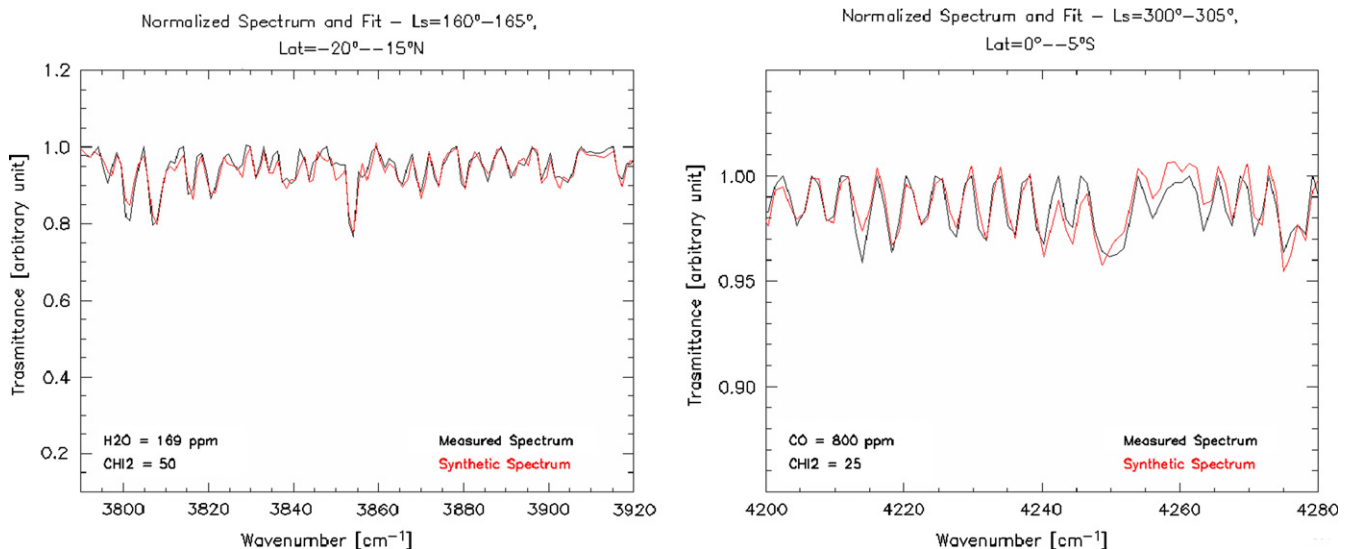
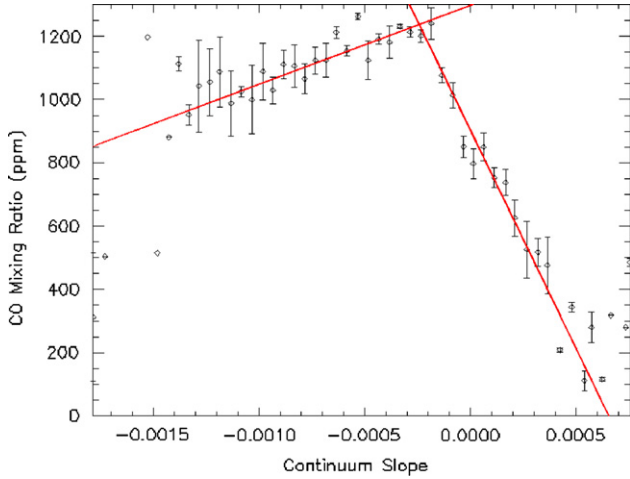


Fig. 5. Spectral fit examples of the water vapour (left) and carbon monoxide (right) absorption bands for averaged spectra (normalized to their continuum) having a minimum  $\chi^2$  of 50 and 25, respectively, which represent the limit values of the selection criterion.



**Fig. 7.** Trend of retrieved CO mixing ratio values on 36174 averaged spectra as a function of the continuum slope (bins of  $5 \times 10^{-5}$ ). Two linear fits are used to find this dependence:  $y_1(m) = 1297.75 + 249272.00m$  for  $m < -2.42 \times 10^{-4}$  and  $y_2(m) = 903.285 - 1.38009e^6m$  for  $m > -2.42 \times 10^{-4}$ . The error bars are calculated as the data standard deviations.

values for slope bins of  $5 \times 10^{-5}$  as a function of the slope. It is clear from the figure that there is a linear relationship between the two quantities described by two linear fits defined as:

$$y(m) = \begin{cases} 1297.75 + 249,272.00m & \text{for } m < -2.42 \times 10^{-4} \\ 903.28 - 1.38e^6m & \text{for } m > -2.42 \times 10^{-4} \end{cases}$$

We have demonstrated that the  $2 \mu\text{m}$  modulation affects the band depth that therefore has to be corrected using the “calibration function”  $y(m)$ .

The corrected mixing ratio value ( $cmr$ ) can be calculated for each data-point as follows:

$$cmr = omr \frac{y(m_{syn})}{y(m)}$$

where  $omr$  is the retrieved mixing ratio value,  $y(m_{syn})$  is the reference mixing ratio (903 ppm) and  $y(m)$  is the mixing ratio value of the calibration function at a considered angular coefficient  $m$ .

The reference mixing ratio  $y(m_{syn})$ , considered as the expected mean value of the whole dataset, has been obtained applying the calibration function to the slope of the continuum of a synthetic spectrum (without modulation) in the CO band.

### 3.6. Evaluation of uncertainties

There are many sources of uncertainties in the procedure described above. First of all, in the synthetic spectra calculation the main error source is the broadening line factor in a  $\text{CO}_2$  dominated atmosphere. Although it is an important parameter, there is little experimental information about its correct value in the considered spectral ranges. The error coming from this factor was evaluated changing its value between 1.3 (Fedorova et al., 2006) and 1.7 (Gamache et al., 1995). In this way we obtained a variation in the retrieved abundance values of about 15% for the  $\text{H}_2\text{O}$  and of about 10% for the CO.

Another source of error has to be found in the used climatic model: the uncertainty derived from the MCD pressure is less than 2%, and the one derived from the MCD temperature is about 5%. For the water vapour analysis, the uncertainty coming from the MCD temperature affects the saturation profile producing an error of about 5% in its abundance.

In order to estimate the uncertainty derived by having neglected the aerosols effect, we have generated a synthetic spectra set, using different dust and ice opacities. The range of variability for the dust

optical depth (at  $1075 \text{ cm}^{-1}$ ) was chosen between 0.05 and 0.4, which represents the Martian mean conditions out of the global dust storm (Smith, 2004; Smith et al., 2009). Processing each spectrum of this set with the analysis procedure used for actual Martian data, we obtained an error (standard deviation of retrieved results) of 7% and 9% in the retrieved concentration for the water vapour and for the carbon monoxide, respectively.

For the variability of the water ice content in the Martian atmosphere, we considered an optical depth range between 0.05 and 0.12 at  $825 \text{ cm}^{-1}$  (Smith, 2004). The ice particle content in the atmosphere results to be totally negligible for the two absorption bands considered in our study.

Another important contribution to the error evaluation derives from the continuum definition: a little variation in its definition and the presence of the instrumental noise can result in errors up to about 5% and 15% in the  $\text{H}_2\text{O}$  and CO concentration, respectively. In addition, only for the CO concentration retrieval, we have to consider the uncertainty due to the “a posteriori correction” for the  $2 \mu\text{m}$  modulation (Section 3.5): the error (standard deviation) is evaluated to be about 5%.

Finally, there is also an intrinsic error in the fit cycle. Since the synthetic spectra are calculated with a minimum step of 5% in the mixing ratio, this value also represents the accuracy of the best fit procedure. Moreover, the fit quality given by the  $\chi^2$  value provides an estimation of the error on concentration of the considered atmospheric component.

Therefore, we can conclude that the broadening line factor and the continuum definition (only for the CO retrieval) represent the main sources of error in the whole procedure. Considering all the contributions, the total error (square sum) for each retrieved concentration value is estimated to be about 19% for the water vapour and about 22% for the carbon monoxide.

## 4. Results

### 4.1. Water vapour: seasonal and geographical behaviour

The water vapour behaviour we retrieve reproduces the well known *seasonal water cycle* in the Mars atmosphere.

In order to come out  $\text{H}_2\text{O}$  results more comparable with other datasets, we converted them in  $\text{pr. } \mu\text{m}$ , taking into account the saturation and pressure profiles. Moreover, since the real vertical distribution of water vapour is still unknown, we applied the topographic correction usually used on the  $\text{H}_2\text{O}$  retrieved values to rule out the topographic effect on the absorption band depth: this effect must be taken into account because the vertical distribution of the water vapour on the Mars atmosphere is non-uniform (Titov et al., 1999). Therefore, this topographic correction is obtained normalizing each column density value to the mean superficial pressure value of 6.1 mbar, i.e. each column density value is multiplied by a  $6.1/p_s$  factor, where  $p_s$  [mbar] is the superficial pressure corresponding to the considered spectrum. This normalization, which seems to give reasonable results, should remove the first-order influence of topography on the retrieved abundances of water vapour.

The retrieved  $\text{H}_2\text{O}$  abundances as a function of Solar Longitude (Ls) and latitude, as observed by PFS/SWC, from orbit 634 to orbit 6537, allow us to study its seasonal cycle. The map obtained, using spectra averaged in  $5^\circ \text{ Ls} \times 5^\circ$  Latitude bins, is shown in Fig. 8.

The mean abundance for the whole dataset results to be about 9.6  $\text{pr. } \mu\text{m}$  with a maximum of 59.0  $\text{pr. } \mu\text{m}$  in correspondence of the summer northern polar cap ( $Ls = 105\text{--}125^\circ$ , Latitude =  $70\text{--}80^\circ\text{N}$ ). The standard deviation over the mean value is about 9.0  $\text{pr. } \mu\text{m}$ . Since the error in estimating the mean water vapour abundance is about 1.8  $\text{pr. } \mu\text{m}$  ( $\ll 9.0 \text{ pr. } \mu\text{m}$ ), the big value of the standard deviation indicates the very large spread in the water vapour abundance values and therefore its variability in the Martian atmosphere. The map shows the

expected water vapour cycle in the Mars atmosphere. The atmospheric content of the water vapour before  $L_s=70^\circ$  begins to increase at middle-high latitudes, between  $40^\circ\text{N}$  and  $70^\circ\text{N}$ , because of the start of the northern polar cap sublimation; then the latitudinal distribution is characterized by a gradient between  $L_s=80^\circ$  and about  $L_s=140^\circ$  (northern summer). During the period  $L_s=130\text{--}150^\circ$  the amount of water vapour at high northern latitudes begins to decrease rapidly. At the same time, a region with relatively high  $\text{H}_2\text{O}$  abundance (about

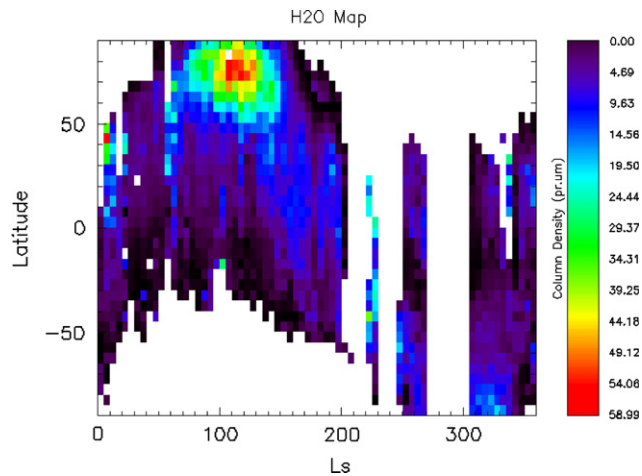


**Fig. 8.** Map of retrieved abundance of water vapour as a function of Solar Longitude ( $L_s$ ) and Latitude as observed by PFS/SWC, from orbit 634 to orbit 6537, obtained using spectra averaged in  $5^\circ L_s \times 5^\circ$  Latitude bins.

$15.9 \text{ pr. } \mu\text{m}$ ) develops at about  $45^\circ\text{N}$ . It moves with season toward the equator reaching it at about  $L_s=190^\circ$  and then it continues to move toward south having a mean value of about  $9.5 \text{ pr. } \mu\text{m}$  from  $L_s=190^\circ$  to  $270^\circ$  (northern fall). During the northern winter (southern summer) for  $L_s=305\text{--}340^\circ$  we can see the increase of the  $\text{H}_2\text{O}$  amount due to the sublimation of the south polar cap ( $70^\circ\text{--}90^\circ\text{S}$ ), with a maximum value of about  $22.8 \text{ pr. } \mu\text{m}$ . Finally, from  $L_s=340^\circ$  the water vapour moves toward north joining at  $L_s=360^\circ$  with the already discussed spring season, starting from  $L_s=0^\circ$ .

In order to study the water vapour distribution in the Martian atmosphere, we used the averaged spectra in square bins of  $10^\circ$  Longitude  $\times$   $10^\circ$  Latitude for each season. The results obtained for  $L_s=0\text{--}90^\circ$  (northern Spring),  $L_s=90\text{--}180^\circ$  (northern Summer),  $L_s=180\text{--}270^\circ$  (northern Fall) and  $L_s=305\text{--}360^\circ$  (northern Winter) are shown in Fig. 9.

We note a peculiarity in almost all the seasons (Spring, Fall and Winter): an increase of the water vapour abundance over two particular regions, Arabia Terra ( $30^\circ\text{E}, 0^\circ\text{N}$ ) and Tharsis ( $100^\circ\text{W}, 0^\circ\text{N}$ ). Both these maxima have been also observed by many instruments and two explanations have been given for them: interaction soil–atmosphere (Smith, 2002) and atmospheric circulation influence with the presence of stationary waves causing a water vapour build-up over certain regions (Fouchet et al., 2007).

It is now interesting to comment on the maximum in the water vapour abundance during the north summer (Fig. 9). Clearly, the biggest  $\text{H}_2\text{O}$  densities are at latitudes between  $60^\circ\text{N}$  and  $85^\circ\text{N}$ , centred around  $75^\circ\text{N}$ . Therefore, the centre of the water distribution is localized out of the permanent polar cap border, which spreads to a latitude of about  $80^\circ\text{N}$ , whereas the seasonal polar cap is already completely withdrawn at  $L_s=90^\circ$ .

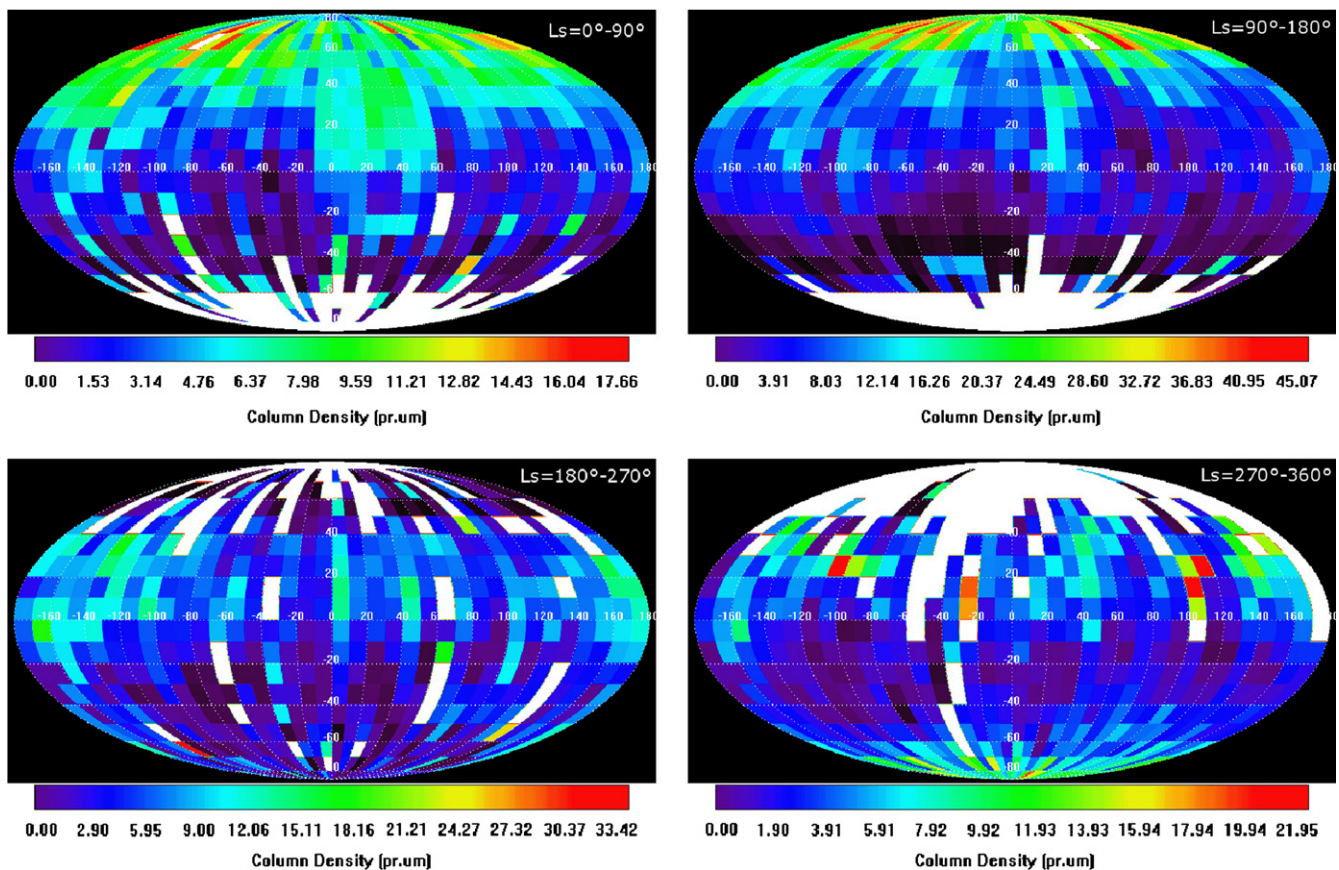


**Fig. 9.** Map of retrieved abundance of water vapour as a function of Longitude and Latitude as observed by PFS/SWC, from orbit 634 to orbit 6537, obtained using averaged spectra in square bins of  $10^\circ$  Longitude  $\times$   $10^\circ$  Latitude for each season:  $L_s=0\text{--}90^\circ$  (northern Spring),  $L_s=90\text{--}180^\circ$  (northern Summer),  $L_s=180\text{--}270^\circ$  (northern Fall) and  $L_s=305\text{--}360^\circ$  (northern Winter).

#### 4.2. Carbon monoxide: seasonal and geographical behaviour

Since the carbon monoxide is assumed to be uniformly distributed in the Mars atmosphere, so being independent on the topography (Smith et al., 2009), we do not need to apply the topographic correction to its concentration values.

The retrieved concentration of carbon monoxide as a function of Solar Longitude (Ls) and latitude, as observed by PFS/SWC, from orbit 634 to orbit 6537, allows us to study its seasonal cycle. The map obtained, using spectra averaged in  $5^\circ$  Ls  $\times$   $5^\circ$  Latitude bins, is shown in Fig. 10.

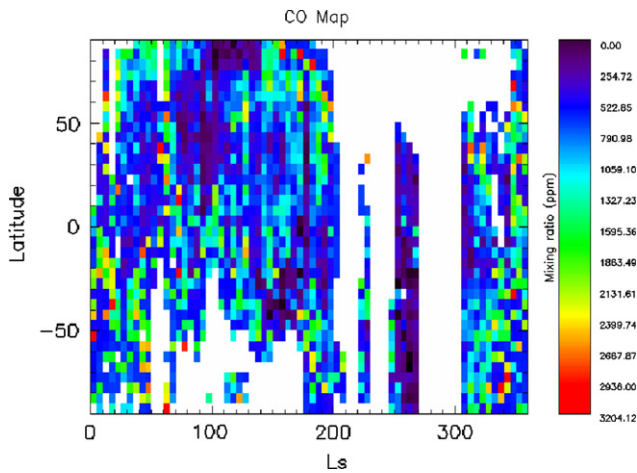


**Fig. 10.** Map of retrieved concentration of carbon monoxide as a function of Solar Longitude (Ls) and Latitude as observed by PFS/SWC, from orbit 634 to orbit 6537, obtained using spectra averaged in  $5^\circ$  Ls  $\times$   $5^\circ$  Latitude bins.

The mean concentration for the whole dataset results to be 990 ppm with a maximum of 3217 ppm. The standard deviation over the mean value is about 580 ppm. Since the error in estimating the mean carbon monoxide concentration is about 220 ppm ( $\leq 580$  ppm), the big value of the standard deviation indicates, also in this case, the large spread (even if less strong than for the  $\text{H}_2\text{O}$ ) in the carbon monoxide concentration values and therefore its variability in the Martian atmosphere. The retrieved CO mixing ratio is noisy because of the weakness of the CO absorption band and the relatively weak dependence of the absorption on CO mixing ratio. For the same reason we have sometimes a bad data coverage, due to the impossibility of having a good fit quality. Despite that, from the map we can see a general seasonal behaviour. Before Ls =  $70^\circ$  there is a CO concentration of about 900 ppm with a definite increase in the middle latitudes of the southern hemisphere and over the north polar cap. From Ls =  $70^\circ$  to  $100^\circ$  the CO mixing ratio decreases over the north polar cap (less than 600 ppm) and its maximum value moves southward. The minimum mean quantity of revealed CO (about 400 ppm or less) is measured between Ls =  $100^\circ$  and  $130^\circ$  over the north polar cap (Latitude =  $75^\circ$ – $90^\circ$ N). In this period it is evident that there is a CO concentration gradient that extends from lower values in the north to higher values (about 980 ppm) in the south. From Ls =  $130^\circ$  to  $190^\circ$  we can observe a new CO maximum zone in the middle-high latitude ( $50$ – $90^\circ$ N): here the mixing ratio values are around 1120 ppm. In the period Ls =  $250$ – $270^\circ$  the south polar cap sublimation causes a CO and non-condensable gases depletion (down to values less than 400 ppm), in an analogous way to what happens in the summer north pole. Finally, from Ls =  $305^\circ$  the CO maximum zone moves toward the equator and at the same time a high CO concentration is evident in the northern hemisphere.

In order to study the carbon monoxide distribution in the Martian atmosphere, we used the averaged spectra in square bin of  $10^\circ$

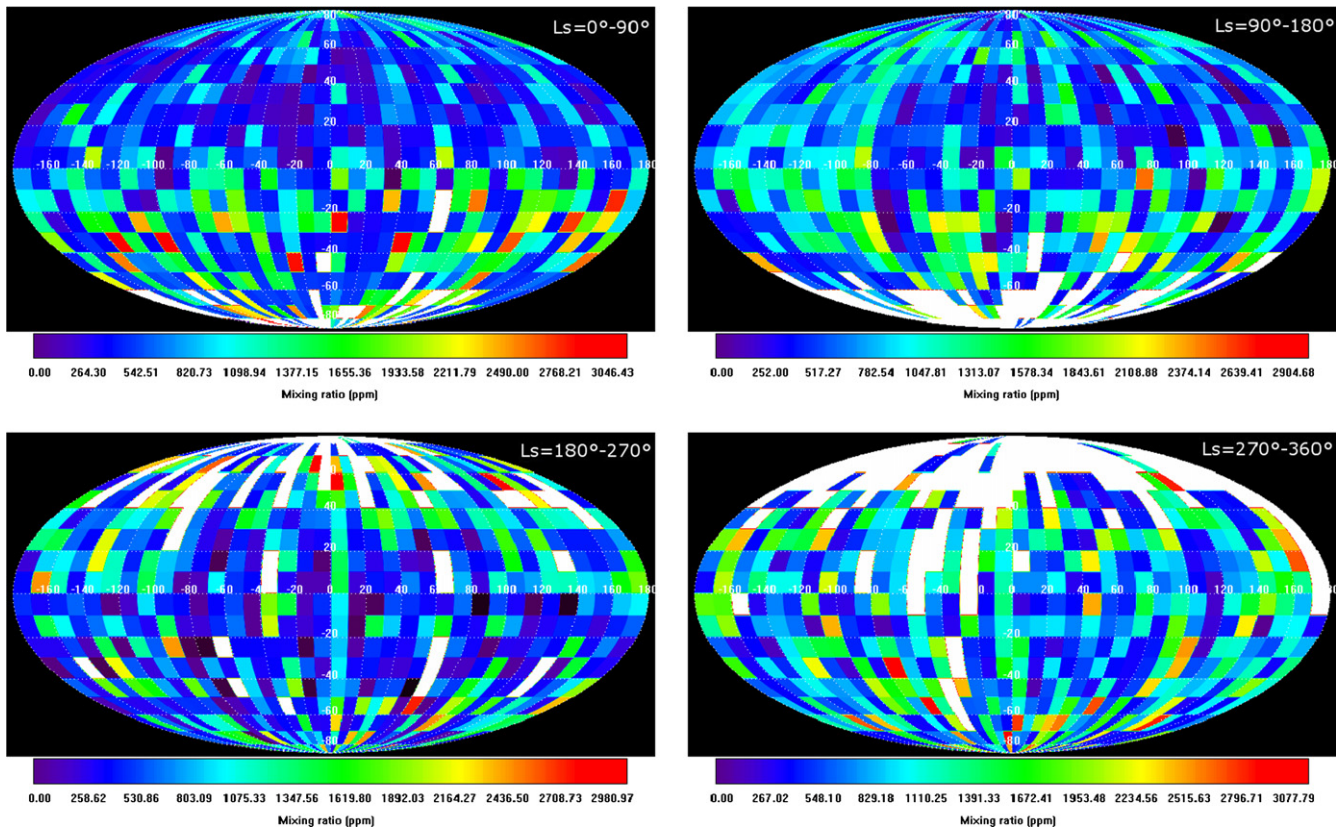


**Fig. 11.** Map of retrieved concentration of carbon monoxide as a function of Longitude and Latitude as observed by PFS/SWC, from orbit 634 to orbit 6537, obtained using averaged spectra in square bins of  $10^\circ$  Longitude  $\times$   $10^\circ$  Latitude for each season: Ls =  $0$ – $90^\circ$  (northern Spring), Ls =  $90$ – $180^\circ$  (northern Summer), Ls =  $180$ – $270^\circ$  (northern Fall) and Ls =  $305$ – $360^\circ$  (northern Winter).

Longitude  $\times 10^\circ$  Latitude for each season. The results obtained for  $L_s=0-90^\circ$  (Spring),  $L_s=90-180^\circ$  (Summer),  $L_s=180-270^\circ$  (Fall) and  $L_s=305-360^\circ$  (Winter) are shown in Fig. 11. The CO geographical variability is characterized by a quite uniform longitudinal distribution, even if it is clear an asymmetry between the two

hemispheres: during northern spring and summer the carbon monoxide is mainly distributed in the southern hemisphere, while during northern fall and winter it has a higher mean concentration in the northern hemisphere. Moreover, no important features seem to indicate an increase over particular geographical regions.

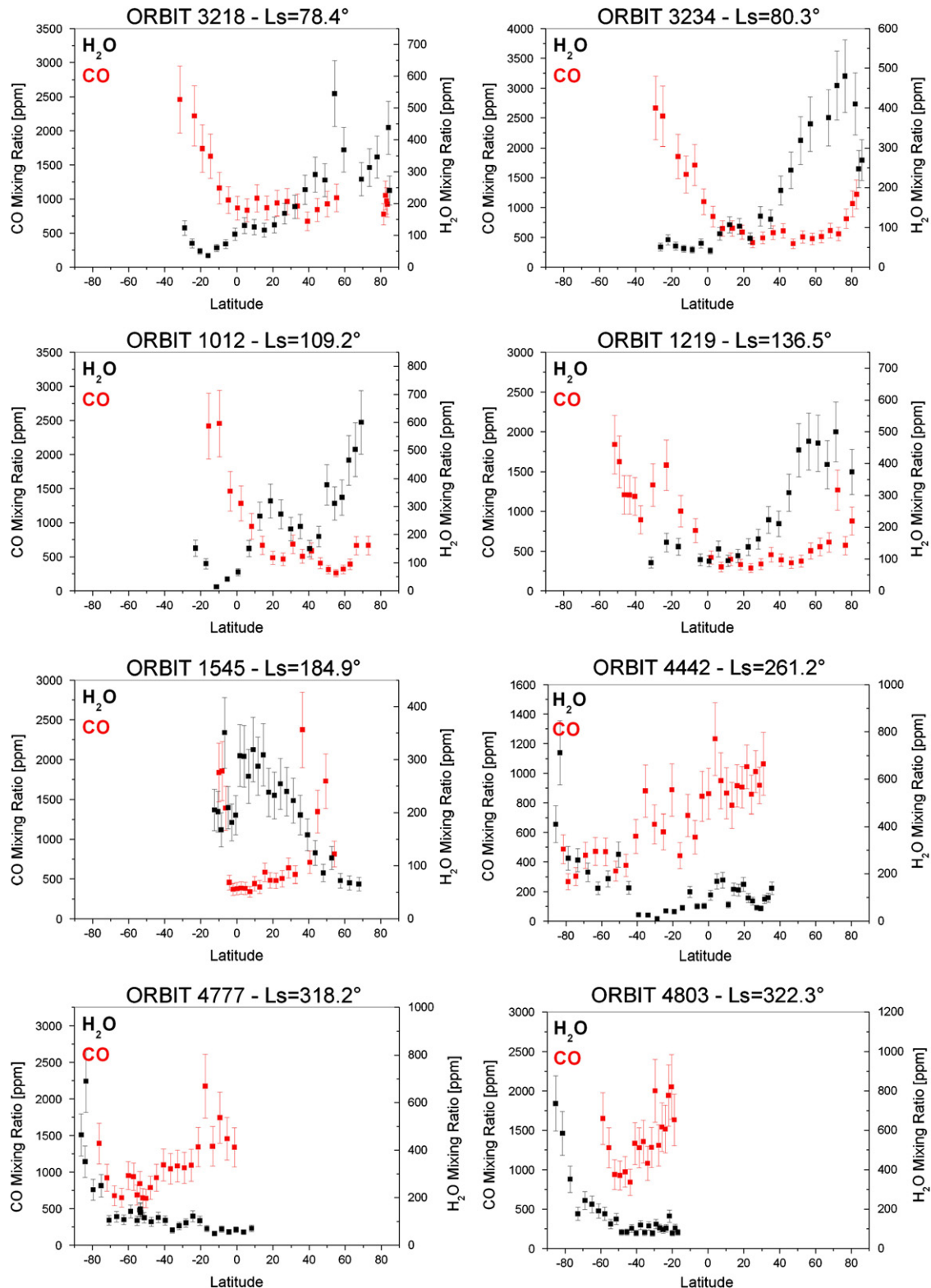


**Fig. 12.** Latitudinal trend of the  $H_2O$  (black) and CO (red) abundances for two orbits of each season: Spring (Orbits 3218, 3234), Summer (Orbits 1012, 1219), Fall (Orbits 1545, 4442) and Winter (Orbits 4777, 4803). (For interpretation of the references to colour in this figure legend, the reader is referred to the web version of this article.)

### 4.3. Comparing H<sub>2</sub>O and CO results

In order to find correlations/anticorrelations in the latitudinal distribution between water vapour and carbon monoxide, we compared the orbital latitudinal trend for a few orbits of each season. For this purpose we used the “orbital dataset” and we expressed both gaseous concentrations in mixing ratios. The orbits selected as examples of the general seasonal latitudinal trend are: 3218 (Ls=78.4°) and 3234 (Ls=80.3°) for northern Spring, 1012 (Ls=109.2°) and 1219 (Ls=136.5°) for northern Summer, 1545 (Ls=184.9°) and 4442 (Ls=261.2°) for northern Fall, and 4777 (Ls=318.2°) and 4803 (Ls=322.3°) for northern Winter. The latitudinal trend of H<sub>2</sub>O and CO concentrations for these orbits is shown in Fig. 12. Choosing individual orbits instead of mean orbital profiles for this kind of study is useful to demonstrate that we are able to maintain a good temporal and spatial resolution in retrieving the gaseous concentrations. The single orbit trends are representative of their own seasonal trends and this is clear comparing them with the averaged ones: in Fig. 13 we show, as examples, the mean latitudinal trends retrieved between Ls=90° and 120° (early northern summer) and between Ls=240° and 270° (late northern fall).

We can start from the first two orbits, 3218 and 3234, examples of the late Spring latitudinal trend. We see the H<sub>2</sub>O enhancement over the northern polar cap region due to the seasonal polar cap sublimation and a corresponding relatively weak depletion of CO in the same region. We find an opposite behaviour in the southern hemisphere, where the coming of the southern polar cap condensation causes an enhancement, as we have already said, of non-condensable gases, including CO, and an H<sub>2</sub>O values of less than 100 ppm in the same region with its maximum centred around 75°N, in agreement with our data obtained analysing the “bin dataset” (Section 4.1).

Following the annual evolution we have the Summer season. For this period we have selected the orbits 1012 and 1219. During the Summer, the latitudinal trend already noticed in the Spring becomes now stronger, as an effect of the more intense north polar cap sublimation and south polar cap condensation processes. For Ls=109.2° (orbit 1012), over the northern polar cap, we find a water vapour maximum of about 600 ppm and lower values of CO mixing ratio (about 550 ppm), while, in the southern hemisphere around 20°S, the CO enhancement and the H<sub>2</sub>O depletion do not seem to be very different than during the Spring season. For Ls=136.5° (orbit 1219) the latitudinal trend becomes weaker again because the water vapour amount begins to move southward, even if the sublimation/condensation processes remain quite evident.

During the Fall season, orbit 1545 shows a relative flattening of the latitudinal distribution of the two gaseous species, even though we can note a weak increase of the CO mixing ratio toward the north pole and of the H<sub>2</sub>O toward the south pole. This trend becomes more clear in the latitudinal distribution of water vapour and carbon monoxide during the late Fall (orbit 4442) and the Winter (orbits 4777 and 4803), when the sublimation of the southern polar cap causes an increase of water vapour (maximum of about 700 ppm at 83°S), while the CO concentration grows northward.

Therefore, from latitudinal orbital study it is possible to confirm the H<sub>2</sub>O and CO seasonal behaviour already shown in the : their tendency is to be generally anticorrelated.

The relationship between water vapour and carbon monoxide in the Mars atmosphere will have a dedicated paper with more details.

## 5. Discussion

The seasonal cycle of water vapour obtained from this analysis was observed also by other instruments, as MAWD (Jakosky and Farmer, 1982), TES (Smith, 2004), SPICAM (Fedorova et al., 2006), PFS/LWC (Fouchet et al., 2007) and PFS/SWC (Tschimmel et al., 2008), and CRISM (Smith et al., 2009). Tschimmel et al. (2008) studied the water vapour distribution during the period between Ls=331° of MY 26 and Ls=196° of MY 27, analysing its 2.6 μm absorption band. Despite their dataset does not overlap in time with ours, it is possible to compare the mean H<sub>2</sub>O behaviour. They observed the maximum value of water vapour abundance of about 60 pr. μm over the sublimating northern polar cap and the typical seasonal cycle, just in agreement with our results. Also their geographical distribution shows the water vapour behaviour we observed, but the local maxima over Arabia Terra and Tharsis are about one and a half time higher than in our maps, while the maxima values, centred around the latitude of 75°N, over the northern polar cap during its summer are in good agreement with our measurements. Since results by Tschimmel et al. (2008) are referred to a period in which the sublimation of the northern polar cap dominates, their average column density of 16.2 pr. μm is higher than our mean value (9.6 pr. μm).

Unfortunately, at the time of this writing only CRISM data can be compared with our data because these are the only data corresponding in time (MY 28–29) to our observations. CRISM measures a water vapour maximum during the northern hemisphere summer at high latitude. Its value is about 50 pr. μm and it is in

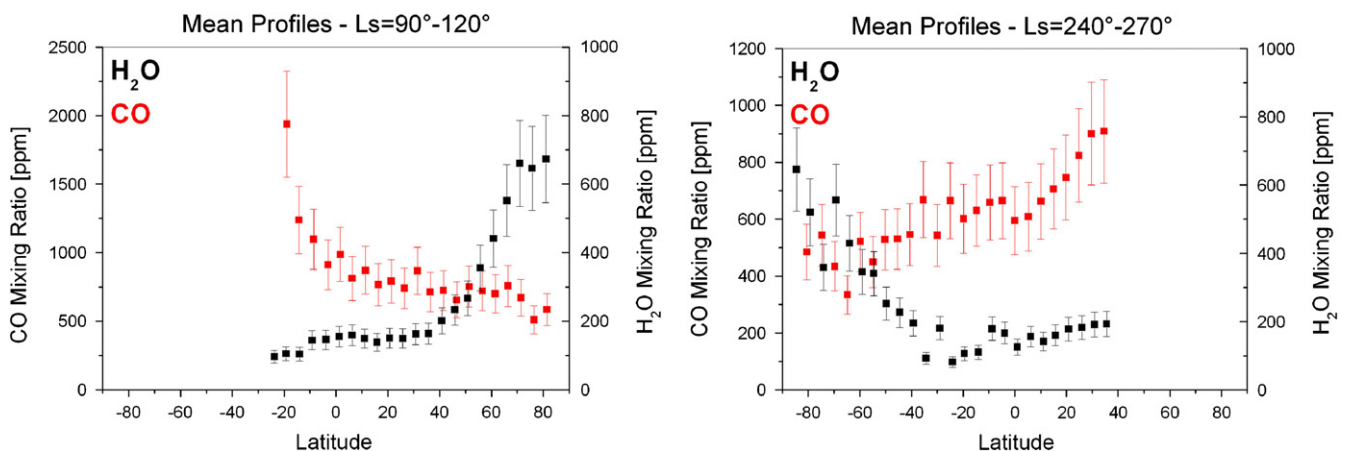


Fig. 13. Examples of mean latitudinal trends retrieved between Ls=90° and 120° (early northern summer) (left) and between Ls=240° and 270° (late northern fall) (right).

agreement with our maximum value of 59 pr.  $\mu\text{m}$ . The location of the centre of the water vapour distribution out of the permanent polar cap border during the northern summer (Section 4.1) is explained by Montmessin et al. (2004) suggestion: the water vapour produced by the seasonal polar cap sublimation is partly carried by the circulation toward the pole and redeposited on the permanent polar cap, whereas the remaining  $\text{H}_2\text{O}$  is carried by the atmospheric dynamics toward the equatorial regions, where it forms the “Equatorial Cloud Belt”. After that, in the centre of the summer (about  $L_s=110^\circ$ ), even the ice created by the  $\text{H}_2\text{O}$  redeposited in the permanent polar cap sublimates, producing the peak that we observe in the maps.

In the southern summer, instead, CRISM data show a reduced water vapour abundance if compared to observations from previous years. These low values are due to the fact that Smith et al. (2009) studied only the MY 28 southern summer: in this year, between  $L_s=270^\circ$  and  $305^\circ$  there was a planet-encircling dust storm, which is known to produce significant changes of the atmospheric state (Smith, 2002) and of the surface albedo (Smith, 2004), resulting in the absence of the southern summer maximum. A similar effect was already noticed by TES data during the MY 25 dust storm (Smith, 2002) and by Viking Orbiter MAWD during the MY 12 dust storm (Fedorova et al., 2004). The normal water vapour trend in the southern hemisphere summer was shown for MY 24–25–26 by TES (Smith, 2002) and for MY 27 by Mars Express SPICAM (Fedorova et al., 2006) and OMEGA (Maltagliati et al., 2008). Our data, out of the global dust storm, show between  $L_s=305^\circ$  and  $340^\circ$  a maximum value of 22.8 pr.  $\mu\text{m}$  over the south polar cap: this lower value compared to the northern summer one is explained by the shorter summer in the southern hemisphere, so the water vapour sublimation is hindered by the presence of a layer of  $\text{CO}_2$  ice for most of the cap. Moreover, also the apparent partial  $\text{H}_2\text{O}$  geographical confinement in the northern hemisphere, probably due to the global circulation, could have a role in this evidence.

The CO seasonal trend as retrieved by our PFS data shows the same latitudinal gradient in the northern hemisphere summer observed by Smith et al. (2009) with CRISM and Krasnopolsky (2003) with the IRTF/CSHELL spectrograph. At  $L_s=112^\circ$  Krasnopolsky measured a CO gradient increasing from north of  $23^\circ\text{N}$  latitude (about 830 ppm) to south (about 1250 ppm at  $45^\circ\text{S}$  latitude), while Smith et al. (2009) revealed a CO mixing ratio gradient from about 450 ppm poleward of  $30^\circ\text{N}$  to 700 ppm at  $30^\circ\text{S}$ . Our measurement provides for the same period a gradient varying from about 270 ppm in the  $75\text{--}90^\circ\text{N}$  latitude to about 1250 ppm in the  $30\text{--}45^\circ\text{S}$  latitude. This hemispheric asymmetry is due to the condensation of the  $\text{CO}_2$  gas in the south polar cap, which would lead to an enhancement in non-condensable gases, such as carbon monoxide, in the southern polar atmosphere. At the same time, the sublimation of the northern polar cap leads to a non-condensable gas depletion causing the strong reduction of the CO mixing ratio. In the same way, but in the opposite hemisphere, during the northern winter we see an enhancement in the CO mixing ratio, while over the south pole we observe a CO depletion due to the ice sublimation. This CO behaviour during the northern winter has also been observed by Billebaud et al. (2009), but they show results for only 90 PFS/MEX orbits, between  $L_s=331.17^\circ$  and  $51.61^\circ$ , measuring 1110 ppm for the CO mixing ratio averaged over their entire data sample. This mean value is slightly higher than the values determined in our and previous works, probably because it refers to a limited dataset. Comparing their CO mixing ratio trends as a function of latitude for three  $L_s$  ranges ( $L_s=331\text{--}360^\circ$ ,  $0\text{--}30^\circ$  and  $30\text{--}52^\circ$ ) with our mean latitudinal trends for the same periods, we find an agreement for the first two trends, although with a 40% higher mean concentration in our data, but an opposite behaviour for the range  $L_s=30\text{--}60^\circ$ . In this period we measure a gradual decrease of the CO concentration between  $40^\circ\text{S}$  and  $0^\circ\text{S}$  in latitude

and a quite constant value of about 1000 ppm going northward up to  $80^\circ\text{N}$ , while Billebaud et al. (2009) reveal a gradual increase up to  $0^\circ$  and a quite constant concentration value around 1000 ppm in the northern hemisphere. These differences could be due to the different dataset analysed and so to the interannual variations in the Mars atmosphere. Billebaud et al. (2009) studied also the trends of the CO mixing ratio as a function of geographical longitude for three latitudinal ranges ( $90^\circ\text{S}\text{--}30^\circ\text{S}$ ,  $30^\circ\text{S}\text{--}30^\circ\text{N}$  and  $30^\circ\text{N}\text{--}90^\circ\text{N}$ ). Comparing these results with our mean trends, we find a very good agreement both in the trends themselves and in the mean concentrations values. Moreover, we observe in the exact same positions the local CO maxima (around  $125^\circ\text{W}$ ,  $50^\circ\text{E}$  and  $150^\circ\text{E}$ ), probably due to planetary waves.

The LMD/GMC model expects that the mixing ratio of non-condensable gases over Hellas basin should reach two times higher values than the mean ones during the summer and a minimum concentration during the winter (Encrenaz et al., 2006). This effect should be due to the isolation of this zone with respect to local vortex. This CO enhancement over Hellas basin has been confirmed by OMEGA/MEX data (Encrenaz et al., 2006) and CRISM/MRO (Smith et al., 2009), but not by the ground-based IRTF/CSHELL data analysed by Krasnopolsky (2003, 2006), which do not show significant variations between the atmosphere in and out the basin. So our observations of the Hellas basin agree with Krasnopolsky's. Moreover, Krasnopolsky (2003) revealed an asymmetry between the northern and southern hemisphere, measuring a CO increasing up to 50% from  $23^\circ\text{N}$  (830 ppm) to  $50^\circ\text{S}$  (1240 ppm). This effect is interpreted as a consequence of the  $\text{CO}_2$  condensation during the polar winter, which leads to an atmospheric enhancement of non-condensable gases. This enhancement effect has also been observed by the Mars Odyssey GRS instrument through the study of argon distribution in the Mars atmosphere (Sprague et al., 2004, 2007). We measure a depletion of about 70% over the summer northern polar cap, while over the summer southern polar cap we find a depletion of about 50% with respect to the planetary mean value. The different weight of the depletion should be due to the different duration of the summer season in the two hemispheres (178 days in the north and 154 days in the south).

The models (Forget et al., 2006; Nelli et al., 2007; Lefèvre and Forget, 2009) also confirmed that the  $\text{CO}_2$  condensation on the winter polar cap causes an increase of the non-condensable gases mixing ratio, and in a similar way, the sublimation from the summer polar cap produces a depletion of non-condensable gases. But, the NASA GCM (General Circulation Model) (Nelli et al., 2007) seems to underestimate the strength and the duration of the depletion, while the LMD model (Forget et al., 2008; Lefèvre and Forget, 2009) seems to underestimate only the duration of the depletion, when these previsions are compared with our data and with CRISM data.

Finally, comparing  $\text{H}_2\text{O}$  and CO results we can conclude that these two gaseous species are generally anticorrelated. The main cause of this anticorrelation is the following: the water vapour being a condensable species and the carbon monoxide a non-condensable one, they are strongly influenced in an opposite way by the processes of condensation and sublimation in the polar caps.

## 6. Conclusions

We have studied the concentration trend of two very important minor species in the Mars atmosphere: water vapour and carbon monoxide. We used observations acquired for more than two and a half Martian years (MY 27–28–29) with Mars Express PFS instrument.

The water vapour retrieval revealed the same seasonal behaviour already observed by TES and other instruments, as PFS and

CRISM. The mean global value is 9.6 pr.  $\mu\text{m}$  and we measure a maximum water vapour concentration of about 59 pr.  $\mu\text{m}$  during the northern summer in the atmosphere over the north polar cap, in agreement with CRISM and all other observational data. After the sublimation of the northern polar cap we observe the water vapour migration toward tropical regions. A similar behaviour is evident in the southern hemisphere: the polar cap sublimation during its summer causes an enhancement of the atmospheric content of water vapour.

Our study of the CO concentrations in the Mars atmosphere led us to observe large variations strictly bound by the condensing and sublimating processes in the polar caps. We measured a mean CO mixing ratio of about 990 ppm, but when the summer polar cap sublimates, releasing CO<sub>2</sub> in the atmosphere, we can see a very strong CO depletion (down to values less than 400 ppm). An opposite behaviour is expected over the winter polar cap, when the CO<sub>2</sub> condenses causing an atmospheric enrichment of non-condensable gases such as carbon monoxide. This trend is indicated by our data, but unfortunately the PFS/SWC can study carbon monoxide only during daytime, thus we have poor information about the atmosphere over the winter polar cap.

Future observations will be useful for a better characterization of the Mars atmospheric composition and climatology. It also will be possible to search for possible new sources and sinks for these gases and their mutual interactions.

## Acknowledgements

The PFS experiment was built at the Istituto di Fisica dello Spazio Interplanetario (IFSI) of Istituto Nazionale di Astrofisica (INAF), and was funded by the Italian Space Agency (ASI) in the context of the Italian participation to the Mars Express mission of ESA. The authors are very grateful to A. Mattana for his data processing support, to N. Ignatiev for code development on synthetic spectra, to D. Grassi, M. Giuranna and M. Tschimmel for valuable discussions.

The authors are grateful to the referees for their very useful corrections and suggestions that improved the paper.

## References

- Altieri, F., Zasova, L., D'Aversa, E., Bellucci, G., Carrozzo, F.G., Gondet, B., Bibring, J.-P., 2009. O<sub>2</sub> 1.27  $\mu\text{m}$  emission maps as derived from OMEGA/MEX data. *Icarus* 204, 499–511.
- Barker, E.S., 1976. Martian atmospheric water vapor observations: 1972–1974 apparition. *Icarus* 28, 247–268.
- Billebaud, F., Brillet, J., Lellouch, E., Fouchet, T., Encrenaz, T., Cottini, V., Ignatiev, N., Formisano, V., Giuranna, M., Maturilli, A., Forget, F., 2009. Observations of CO in the atmosphere of Mars with PFS onboard Mars Express. *Planet. Space Sci.* 57, 1446–1457.
- Clancy, R.T., Wolff, M.J., Christensen, P.R., 2003. Mars aerosol studies with the MGS TES emission phase function observations: optical depths, particle sizes, and ice cloud types versus latitude and solar longitude. *J. Geophys. Res.* 108 (E9).
- Comolli, L., Saggin, B., 2005. Evaluation of the sensitivity to mechanical vibrations of an IR Fourier spectrometer. *Rev. Sci. Instrum.* 76 (12), 123112.
- Encrenaz, T., Melchiorri, R., Fouchet, T., Drossart, P., Lellouch, E., Gondet, B., Bibring, J.-P., Langevin, Y., Titov, D., Ignatiev, N., Forget, F., 2005. A mapping of Martian water sublimation during early northern summer using OMEGA/Mars Express. *Astron. Astrophys.* 441, L9L12.
- Encrenaz, T., Fouchet, T., Melchiorri, R., Drossart, P., Gondet, B., Langevin, Y., Bibring, J.-P., Forget, F., Bézard, B., 2006. Seasonal variation of the Martian CO over Hellas as observed by OMEGA/Mars Express. *Astron. Astrophys.* 459, 265–270.
- Encrenaz, T., Greathouse, T.K., Richter, M.J., Bézard, B., Fouchet, T., Lefèvre, F., Montmessin, F., Forget, F., Lebonnois, S., Atreya, S.K., 2008. Simultaneous mapping of H<sub>2</sub>O and H<sub>2</sub>O<sub>2</sub> on Mars from infrared high-resolution imaging spectroscopy. *Icarus* 195, 547–556.
- Esposito, F., Giuranna, M., Maturilli, A., Palomba, E., Colangeli, L., Formisano, V., 2006. Albedo and photometric study of Mars with the Planetary Fourier Spectrometer on-board the Mars Express mission. *Icarus* 186, 527–546.
- Fast, K.E., Kostiuik, T., Lefèvre, F., Hewagama, T., Livengood, T.A., Delgado, J.D., Annen, J., Sonnabend, G., 2009. Comparison of HIPWAC and Mars Express SPICAM observations of ozone on Mars 2006–2008 and variation from 1993 IRHS observations. *Icarus* 203, 20–27.
- Fedorova, A.A., Rodin, A.V., Baklanova, I.V., 2004. MAWD observations revisited: seasonal behavior of water vapor in the Martian atmosphere. *Icarus* 171, 54–67.
- Fedorova, A.A., Korablev, O., Bertaux, J.-L., Rodin, A., Kiselev, A., Perrier, S., 2006. Mars water vapor abundance from SPICAM IR spectrometer: seasonal and geographic distributions. *J. Geophys. Res.* 111, E09S08. doi:10.1029/2006JE002695.
- Fiorenza, C., Formisano, V., 2005. A solar spectrum for PFS data analysis. *Planet. Space Sci.* 53, 1009–1016.
- Forget, F., Montabone, L., Lebonnois, S., 2006. Non-condensable gas enrichment and depletion in the Martian polar regions. In: *Proceedings of the Second Workshop on Mars Modeling and Observations*, Granada, Spain.
- Forget, F., Millour, E., Montabone, L., Lefèvre, F., 2008. Noncondensable gas enrichment and depletion in the Martian polar regions. In: *Proceedings of the Third Workshop on Mars Modeling and Observations*, Williamsburg, Virginia.
- Formisano, V., Grassi, D., Orfei, R., Biondi, D., Mencarelli, E., Mattana, A., Nespoli, F., Maturilli, A., Giuranna, M., Rossi, M., Maggi, M., Baldetti, P., Chionchio, G., Saggin, B., Angrilli, F., Bianchini, G., Piccioni, G., di Lellis, A., Cerroni, P., Capaccioni, F., Capria, M.T., Coradini, A., Fonti, S., Orofino, V., Blanco, A., Colangeli, L., Palomba, E., Esposito, F., Patsaev, D., Moroz, V., Zasova, L., Ignatiev, N., Khatuntsev, I., Moshkin, B., Ekonomov, A., Grigoriev, A., Nechaev, V., Kiselev, A., Nikolsky, Y., Gnedych, V., Titov, D., Orleanski, P., Rataj, M., Malgoska, M., Jurewicz, A., Blecka, M.I., Hirsh, H., Arnold, G., Lellouch, E., Marten, A., Encrenaz, T., Lopez Moreno, J., Atreya, S., Gobbi, P., 2004. PFS: the Planetary Fourier Spectrometer for Mars Express. In: Wilson, A., Chicarro, A. (Eds.), *ESA Special Publication*, vol. 1240. ESA Publications Division, Noordwijk, pp. 71–94.
- Formisano, V., Angrilli, F., Arnold, G., Atreya, S., Bianchini, G., Biondi, D., Blanco, A., Blecka, M.I., Coradini, A., Colangeli, L., Ekonomov, A., Esposito, F., Fonti, S., Giuranna, M., Grassi, D., Gnedych, V., Grigoriev, A., Hansen, G., Hirsh, H., Khatuntsev, I., Kiselev, A., Ignatiev, N., Jurewicz, A., Lellouch, E., Lopez Moreno, J., Marten, A., Mattana, A., Maturilli, A., Mencarelli, E., Michalska, M., Moroz, V., Moshkin, B., Nespoli, F., Nikolsky, Y., Orfei, R., Orleanski, P., Orofino, V., Palomba, E., Patsaev, D., Piccioni, G., Rataj, M., Rodrigo, R., Rodriguez, J., Rossi, M., Saggin, B., Titov, D., Zasova, L., 2005. The Planetary Fourier Spectrometer (PFS) onboard the European Mars Express mission. *Planet. Space Sci.* 53, 963–974.
- Fouchet, T., Lellouch, E., Ignatiev, N.I., Titov, D., Tschimmel, M., Formisano, V., Giuranna, M., Maturilli, A., Encrenaz, T., 2007. Martian water vapor: Mars Express PFS/LW observations. *Icarus* 190, 32–49.
- Gamache, R.R., Neshyba, S.P., Plateaux, J.J., Barbe, A., Régalia, L., Pollack, J.B., 1995. CO<sub>2</sub>-broadening of water-vapor lines. *J. Mol. Spectrosc.* 170, 131–151.
- Giuranna, M., Formisano, V., Biondi, D., Ekonomov, A., Fonti, S., Grassi, D., Hirsch, H., Khatuntsev, I., Ignatiev, N., Michalska, M., Mattana, A., Maturilli, A., Moshkin, B.E., Mencarelli, E., Nespoli, F., Orfei, R., Orleanski, P., Piccioni, G., Rataj, M., Saggin, B., Zasova, L., 2005. Calibration of the Planetary Fourier Spectrometer short wavelength channel. *Planet. Space Sci.* 53, 975–991. doi:10.1016/j.pss.2004.12.007.
- Giuranna, M., Hansen, G., Maturilli, A., Zasova, L., Formisano, V., Grassi, D., Ignatiev, N., 2007. Spatial variability, composition and thickness of the seasonal north polar cap of Mars in mid-spring. *Planet. Space Sci.* 55, 1328–1345. doi:10.1016/j.pss.2007.03.006.
- Hansen, G.B., 1999. Control of the radiative properties of the Martian polar caps by surface CO<sub>2</sub> ice: evidence from Mars Global Surveyor measurements. *J. Geophys. Res.* 104, 16471–16486.
- Ignatiev, N.I., Grassi, D., Zasova, L.V., 2005. Planetary Fourier spectrometer data analysis: fast radiative transfer models. *Planet. Space Sci.* 53, 1035–1042. doi:10.1016/j.pss.2004.12.009.
- Jakosky, B.M., Farmer, C.B., 1982. The seasonal and global behaviour of water vapor in the Mars atmosphere—complete global results of the Viking atmospheric water detector experiment. *J. Geophys. Res.* 87, 2999–3019.
- Krasnopolsky, V.A., 1995. Uniqueness of a solution of a steady-state photochemical problem: applications to Mars. *J. Geophys. Res.* 100, 3263–3276.
- Krasnopolsky, V.A., 2003. Spectroscopic mapping of Mars CO mixing ratio: detection of north-south asymmetry. *J. Geophys. Res.* 108 (E2), 5010.
- Krasnopolsky, V.A., 2006. Long-term spectroscopic observations of latitudinal and seasonal variations of O<sub>2</sub> dayglow and CO on Mars. *Icarus* 190, 93–102.
- Lefèvre, F., Forget, F., 2009. Observed variations of methane on Mars unexplained by known atmospheric chemistry and physics. *Nature* 460, 720–723. doi:10.1038/nature08228.
- Maltagliati, L., Titov, D.V., Encrenaz, T., Melchiorri, R., Forget, F., Garcia-Comas, M., Keller, H.U., Langevin, Y., Bibring, J.-P., 2008. Observations of atmospheric water vapor above the Tharsis volcanoes on Mars with the OMEGA/MEX imaging spectrometer. *Icarus* 194, 53–64.
- Marti, J., Mauersberger, K., 1993. A survey and new measurements of ice vapor pressure at temperature between 170 and 250 K. *Geophys. Res. Lett.* 20, 363–366.
- Melchiorri, R., Encrenaz, T., Fouchet, T., Drossart, P., Lellouch, E., Gondet, B., Bibring, J.-P., Langevin, Y., Schmitt, B., Titov, D., Ignatiev, N., 2007. Water vapor mapping on Mars using OMEGA/Mars Express. *Planet. Space Sci.* 55, 333–342.
- Montmessin, F., Forget, F., Rannou, P., Cabane, M., Haberle, R.M., 2004. Origin and role of water ice clouds in the Martian water cycle as inferred from a general circulation model. *J. Geophys. Res.* 109, 10004.
- Nair, H., Allen, M., Anbar, A.D., Yung, Y.L., Clancy, R.T., 1994. A photochemical model of the Martian atmosphere. *Icarus* 111, 124–150.

- Nelli, S.M., Murphy, J.R., Sprague, A.L., Boynton, W.V., Kerry, K.E., Janes, D.M., Metzger, A.E., 2007. Dissecting the polar dichotomy of the noncondensable gas enhancement on Mars using the NASA Ames Mars General Circulation Model. *J. Geophys. Res.* 112, E08S91. doi:10.1029/2006JE002849.
- Ockert-Bell, M.E., Bell, J.F., Pollack, J.B., McKay, C.P., Forget, F., 1997. Absorption and scattering properties of the Martian dust in the solar wavelengths. *J. Geophys. Res.* 102 (E4), 9039–9050.
- Rosenqvist, J., Drossart, P., Combes, M., Encrenaz, T., Lellouch, E., Bibring, J.P., Erard, S., Langevin, Y., Chassefière, E., 1992. Minor constituents in the Martian atmosphere from the ISM/Phobos experiment. *Icarus* 98, 254–270.
- Rothman, et al., 2005. The HITRAN 2004 molecular spectroscopic database. *J. Quant. Spectrosc. Radiat. Transfer* 96, 139–204.
- Smith, M.D., 2002. The annual cycle of water vapor as observed by the Thermal Emission Spectrometer. *J. Geophys. Res.* 107. doi:10.1029/2001JE001522.
- Smith, M.D., 2004. Interannual variability in TES atmospheric observations of Mars during 1999–2003. *Icarus* 167, 148–165.
- Smith, M.D., 2008. Mars water vapor climatology from MGS/TES. Mars Water Cycle Workshop, April 2008, Paris, France (abstract).
- Smith, M.D., Wolff, M.J., Clancy, R., T., Murchie, S.L., 2009. Compact Reconnaissance Imaging Spectrometer observations of water vapor and carbon monoxide. *J. Geophys. Res.* 114, E00D03. doi:10.1029/2008JE003288.
- Spinrad, H., Munch, G., Kaplan, L.D., 1963. Letter to the Editor: the detection of water vapor on Mars. *Astrophys. J.* 137, 13–19.
- Sprague, A.L., Boynton, W.V., Kerry, K.E., Janes, D.M., Hunten, D.M., Kim, K.J., Reedy, R.C., Metzger, A.E., 2004. Mars' south polar Ar enhancement: a tracer for south polar seasonal meridional mixing. *Science* 306, 1364–1367.
- Sprague, A.L., Boynton, W.V., Kerry, K.E., Janes, D.M., Kelly, N.J., Crombie, M.K., Nelli, S.M., Murphy, J.R., Reedy, R.C., Metzger, A.E., 2007. Mars' atmospheric argon: tracer for understanding Martian atmospheric circulation and dynamics. *J. Geophys. Res.* 112, E03S02. doi:10.1029/2005JE002597.
- Titov, D.V., Markiewicz, W.J., Thomas, N., Keller, H.U., Sablotny, R.M., Tomasko, M.G., Lemmon, M.T., Smith, P.H., 1999. Measurements of the atmospheric water vapor on Mars by the Imager for Mars Pathfinder. *J. Geophys. Res.* 104, 9019–9026.
- Tschimmel, M., Ignatiev, N.I., Titov, D., Lellouch, E., Fouchet, T., Giuranna, M., Formisano, V., 2008. Investigation of the water vapour on Mars with PFS/SW of Mars Express. *Icarus* 195, 557–575.